



FeCo/FeCoNi/N-doped carbon nanotubes grafted polyhedron-derived hybrid fibers as bifunctional oxygen electrocatalysts for durable rechargeable zinc–air battery



Zhe Wang^a, Jiaming Ang^a, Bowei Zhang^a, Youfang Zhang^a, Xiu Yun Daphne Ma^a, Tao Yan^b, Jian Liu^a, Boyang Che^a, Yizhong Huang^a, Xuehong Lu^{a,*}

^a School of Materials Science and Engineering, Nanyang Technological University, 50 Nanyang Avenue, 639798, Singapore

^b College of Textile and Clothing Engineering, Soochow University, Suzhou, 215123, China

ARTICLE INFO

Keywords:

Hybrid porous carbon fiber
Bifunctional oxygen electrocatalysts
FeCo and FeCoNi alloys
Self-supported air cathode
Zn-air battery

ABSTRACT

The rational design and exploration of highly efficient, low-cost, and robust electrocatalysts for oxygen reduction reaction (ORR) and oxygen evolution reaction (OER) is critical for development of rechargeable metal-air batteries. Herein, we report a novel approach for the synthesis of bifunctional electrocatalysts, where $\text{Fe}_{0.5}\text{Co}_{0.5}$ and $\text{Fe}_{0.5}\text{Co}_{0.4}\text{Ni}_{0.1}$ alloys are encapsulated in the nitrogen-doped carbon nanotubes-grafted porous polyhedron-derived hybrid fibers (FeCo/FeCoNi@NCNTs-HF). Benefiting from its hierarchically porous structure and strong synergistic coupling among FeCo, FeCoNi alloys, and N-doped carbon species. The obtained electrocatalyst exhibits a positive half-wave potential of 0.850 V for ORR and a low potential of 1.608 V to achieve a current density of 10 mA cm^{-2} for OER, as well as superior stability in alkaline media. As a demonstration, FeCo/FeCoNi@NCNTs-HF is employed as the electrocatalysts in the air cathode of a Zn-air battery, which shows superior discharge and charge performance, large power density, high specific capacity, and outstanding cycling stability of 240 h (360 cycles). More impressively, excellent cyclability with a lifetime of 670 h (1005 cycles) is also achieved by the Zn-air battery with FeCo/FeCoNi@NCNTs-HF as the self-supported air electrode. This work will open a novel avenue to develop advanced bifunctional electrocatalysts for the next generation of metal-air batteries.

1. Introduction

Rechargeable metal-air batteries have attracted extensive attention as a class of renewable energy storage devices owing to their high energy density, low cost, superior safety and environmental friendliness [1–3]. Oxygen reduction reaction (ORR) and oxygen evolution reaction (OER) are the two essential electrochemical reactions responsible for the operation of these batteries, which hence require highly efficient ORR and OER electrocatalysts as the critical components of their air cathodes [4–7]. To date, platinum (Pt) is the most efficient electrocatalyst for ORR, while ruthenium (Ru)/iridium (Ir) oxides ($\text{RuO}_2/\text{IrO}_2$) exhibit the best electrocatalytic performance for OER [4,8,9]. An individual noble metal-based catalyst alone cannot, however, effectively and stably catalyze both ORR and OER. In addition, the scarcity and high cost of these precious metals further hamper their usage for large-scale industrial applications [10,11]. Therefore, alternative low-cost electrocatalysts with high activity towards both ORR and OER are

highly desired.

During the past decades, many kinds of efficient and earth-abundant electrocatalysts, including transition metals such as iron (Fe), cobalt (Co), nickel (Ni) and their alloys, metal-free heteroatom-doped carbon materials, as well as perovskites, etc., have been developed for ORR and OER electrocatalysis [12–17]. Among them, carbon materials doped with transition metal alloys have been identified as one of the most promising candidates for ORR and OER electrocatalysts [18–20] because the bonds between the metals can constitute intrinsic polarity and provide multiple valence states, significantly promoting ORR and OER [21]. Recent studies also demonstrated that the integration of transition-metal-alloy nanoparticles (NPs) with heteroatom (N, P, or S)-doped porous carbon matrices could further enhance their electrocatalytic performance [22–25]. This is due to the fact that these porous carbon materials typically have high electrical conductivity, and yet possess high porosity and large specific surface area, which increase the exposure of active sites to electrolytes, enhance mass transport of the

* Corresponding author.

E-mail address: asxhlu@ntu.edu.sg (X. Lu).

electrolyte and reactants, and efficiently prevent the aggregation of the alloy NPs [27–29]. More importantly, the synergy among different types of transition metals, heteroatom-containing species and porous carbon frameworks can enrich localized active catalytic sites, as well as modify their electronic structures to reduce the kinetic energy barriers and accelerate charge transfer, thereby further promoting the bifunctional electrocatalytic processes [21,26,29].

To fabricate transition metal alloy and heteroatom co-doped porous carbon frameworks with desired structures and morphologies, a popular approach is to utilize porous organic-inorganic hybrid materials as precursors [30–32]. Among various hybrid porous materials, Prussian blue (PB) and its analog (PBA), which are a class of metal-organic frameworks (MOFs), have recently emerged as attractive precursors for the synthesis of the highly porous carbon frameworks owing to their intrinsic advantages of tailorable geometry, compositional flexibility, abundant pores and hierarchical pore structure, as well as high specific surface area [33–36]. In particular, the good compatibility of PB/PBA with various metal ions offers a unique benefit to material synthesis, i.e., allowing the controlled integration of bi or even multiple metallic species in the same framework. This may improve the electrocatalytic property of the materials by the synergistic effects of various metallic species and multiple valencies of the contributing metals [37,38]. Furthermore, the hierarchical porous nanostructures of the final products can be tuned by rationally selecting components and synthesis methods, as well as the subsequent transformation processes. The PB/PBA-based materials, however, also have their own limitation, namely, the lack of interconnectivity among the crystalline polyhedrons caused by their powdery nature, which render their carbonized products difficult to form robust, flexible superstructures as self-supported electrocatalysts, limiting their adaptation for practical metal-air batteries.

To overcome the limitation mentioned above, herein we present a new strategy to synthesize highly active yet durable bifunctional electrocatalysts by incorporating FeCo and FeCoNi alloys into a N-doped carbon nanotubes-grafted porous polyhedron-derived hybrid fiber (FeCo/FeCoNi@NCNTs-HF) via electrospinning and subsequent calcination. Benefiting from the high catalytic activities provided by abundant FeCo and FeCoNi NPs in the N-doped carbon matrix, the hierarchically porous structures that could increase the exposure of active sites and expedite the transport of intermediates, and large specific surface area, the optimized electrocatalyst exhibits outstanding electrocatalytic activities and stabilities toward both ORR and OER, which are comparable to those of commercial Pt/C (for ORR) and RuO₂ (for OER) catalysts. Impressively, the FeCo/FeCoNi@NCNTs-HF catalyst shows remarkable rechargeability and long-term cyclability as an air electrode in a Zn-air battery system. Moreover, owing to its flexibility and robustness, the FeCo/FeCoNi@NCNTs-HFs can also act as a flexible self-supported air cathode in Zn-air batteries. The findings from this work will shed new light on the rational design of highly efficient and durable bifunctional electrocatalysts for rechargeable Zn-air batteries.

2. Experimental section

2.1. Materials

Polyacrylonitrile (PAN, M_w = 150,000 g mol⁻¹, Sigma-Aldrich), N,N-dimethylformamide (DMF, M_w = 73.09 g mol⁻¹, Sigma-Aldrich), trisodium citrate dehydrate (M_w = 294.10 g mol⁻¹, Sigma-Aldrich), cobalt(II) acetate tetrahydrate (98.0%, Energy Chemical), potassium hexacyanoferrate(III) (99.95%, Aladdin), Nickel(II) nitrate hexahydrate (Ni(NO₃)₂·6H₂O, ≥97.0%, Sigma-Aldrich), Melamine (M_w = 126.12 g mol⁻¹, Sigma-Aldrich), Nafion (5 wt% in alcohol and water, Sigma-Aldrich), commercial platinum/carbon (Pt/C) 20 wt% (Pt on carbon black, Premetek Co.), ruthenium oxide (RuO₂, Sigma-Aldrich). All chemicals were used as received without further purification.

2.2. Synthesis of the KFeCo PBA OFS

The synthesis method of the KFeCo combined Prussian blue analogs with an open frame-like structure (KFeCo PBA OFSs) is similar to previous reported one with small modification [39]. Typically, 0.75 g cobalt(II) acetate tetrahydrate and 0.73 g trisodium citrate dehydrate were dissolved in 100 ml deionized (DI) water (18.2 Ω) to form solution A. 0.50 g Potassium hexacyanoferrate(III) was dissolved in 150 ml DI water to form solution B. Then, solution B was added into solution A under magnetic stirring. After continuous stirring for 1 min, the obtained mixed solution was aged at 40 °C for 40 h. The precipitate was collected by centrifugation, washed with DI water, and dried at 70 °C overnight.

2.3. Synthesis of the FeCo/FeCoNi@NCNTs-HFs

The FeCo/FeCoNi@NCNTs-HFs were prepared through a simple electrospinning technique followed by heat treatment. As optimization of synthetic conditions, 0.3 g Ni(NO₃)₂·6H₂O and 1.2 g Fe-Co PBA NAFSs were dissolved in 5 ml DMF with stirring to obtain a homogeneous solution. Then 0.5 g PAN was dissolved in the mixed solution under magnetic stirring at room temperature until to get uniform solution. The precursor solution for electrospinning was obtained. The precursor solution was transferred into a 10 ml plastic syringe with a metal needle. The electrospinning instrument was shown in **Scheme 1**, in a typically electrospinning process, a high voltage of 19 kV was applied at needle tip with the flow rate of solution set to be 1 ml h⁻¹, and the distance between the needle tip and collector was 12 cm. An aluminium foil used as the receiving plate to collect fibres. The as-prepared fibrous membrane was dried at 70 °C in a vacuum oven for 12 h. Thereafter, the composite fibre mat was transferred to a tube furnace to be heated under argon (Ar) environment at the following procedure: firstly heated at rate of 1 °C min⁻¹ from room temperature to 250 °C, and maintained for 1 h, then heated at rate of 2 °C min⁻¹ from 250 °C to 550 °C, and maintained for 1 h, followed by heating at rate of 5 °C min⁻¹ from 550 °C to a target temperature (800, 900 and 1000 °C), and maintained for 2 h. The obtained FeCo and FeCoNi alloys decorated carbon fibers were denoted as FeCo/FeCoNi@HF-X (X representing the final annealing temperature in Ar atmosphere). Finally, the resulting hybrid FeCo/FeCoNi@HF-900 membrane and melamine with a mass ratio of 1:10 were further pyrolyzed at 900 °C for 2 h in the nitrogen (N₂) flow (denoted as FeCo/FeCoNi@NCNTs-HF). In addition, FeCo@HF-900 was also prepared as a control sample using the same fabrication procedure of FeCo/FeCoNi@HF-900 only without adding Ni (NO₃)₂·6H₂O in electrospun precursor solution. The FeCo@NCNTs-HF was prepared by further annealing FeCo@HF-900 in the presence of melamine (using the same fabrication procedure of FeCo/FeCoNi@NCNTs-HF) at 900 °C for 2 h under nitrogen atmosphere.

2.4. Materials characterization

The morphological information of all the samples was examined with Field-emission scanning electron microscopy (FESEM; JEOL, JSM-6701 F). Transmission electron microscopy (TEM), high resolution TEM (HRTEM), and elemental mapping were performed using a JEM-2010 F instrument. X-ray diffraction (XRD) patterns were obtained by a RigaKu MiniFlex 600 I diffractometer equipped with Cu K α radiation (λ = 1.5406 Å). Raman spectra are collected using a LabRAM HR instrument with a 632 nm excitation laser. The Brunauer-Emmett-Teller (BET) specific surface area and porous structure were measured at 77 K by a Micromeritics ASAP 2020 system. X-ray photoelectron spectroscopy (XPS) analysis was carried out on a Kratos Axis Ultra DLD electron spectrometer to analyze chemical elements and chemical configuration, and the binding energy was calibrated by means of the C 1s peak energy of 284.8 eV.

2.5. Electrochemical measurements

Electrochemical measurements were performed on an Autolab workstation (Autolab Instrument) equipped with high-speed rotators from Pine Instruments (PINE Research Instrumentation) at room temperature. A typical three-electrode system was employed, including a commercial glassy carbon (GC) electrode (5 mm diameter, 0.19625 cm²) as the working electrode, a platinum foil and Ag/AgCl electrode in 3 M KCl solution serve as the counter and reference electrodes, respectively. The catalyst ink was prepared by dispersing 5 mg of the as-prepared powdered catalyst in 1 ml of mixed solution containing 0.98 ml of ethanol/water (1:1, v/v) and 20 μL of 5 wt% Nafion solution, followed by ultra-sonication for 30 min to obtain a homogeneous black suspension solution. Afterward, the catalyst ink was dropped onto the GC to give a loading amount of 0.60 mg cm⁻² for the developed catalysts. For comparison, the commercial Pt/C (20 wt%) or RuO₂ were used as reference catalysts with the loading amount of 0.30 mg cm⁻². All the measured potentials against Ag/AgCl in this study were referenced to the reversible hydrogen electrode (RHE) based on the following conversion equation:

$$E_{\text{RHE}} = E_{\text{Ag/AgCl}} + 0.21 + 0.059 \times \text{pH} \quad (1)$$

where E_{RHE} is the converted potential versus RHE, $E_{\text{Ag/AgCl}}$ is the experimental potential measured against the Ag/AgCl reference electrode.

All the measurements were carried out in 0.1 M KOH solution. For ORR, the cyclic voltammetry (CV) curves were obtained in N₂ and O₂ saturated 0.1 M KOH with a scan rate of 50 mV s⁻¹. Linear sweep voltammetry (LSV) were performed in O₂ saturated 0.1 M KOH using rotating disk electrode (RDE) at a scan rate of 5 mV s⁻¹ and various rotation speeds (400, 625, 900, 1225 and 1600 rpm). The electron transfer number during ORR was calculated by Koutecky-Levich (K-L) equation:

$$\frac{1}{j} = \frac{1}{j_k} + \frac{1}{B\omega^{1/2}} \quad (2)$$

$$B = 0.62nFC_0D_0^{2/3}\nu^{-1/6} \quad (3)$$

where j is the measured current density on RDE, j_k is the kinetic current density, B is the reciprocal of the slope, ω is the angular velocity, n is transferred electron number, F is Faraday constant (96485 C mol⁻¹), C_0 is the saturated concentration of O₂ in 0.1 M KOH (1.2×10^{-6} mol cm⁻³), D_0 is the diffusion coefficient of O₂ in 0.1 M KOH (1.9×10^{-5} cm² s⁻¹), and ν is the kinetic viscosity of 0.1 M KOH (0.01 cm² s⁻¹). The ORR stability tests were performed by chronoamperometric measurements at a potential of 0.80 V (vs. RHE) in O₂ saturated 0.1 M KOH solution.

The electrochemically active surface area (ECSA) values of different samples were evaluated by double layer capacitance (C_{dl}). The C_{dl} was tested via CVs of samples at various scan rates (5, 10, 20, 30, 40, and 60 mV s⁻¹). The C_{dl} was obtained by plotting $(j_a - j_c)$ at 1.10 V vs. RHE (where j_a and j_c are the anodic and cathodic current densities, respectively) against the scan rates. The slope of the above profiles was twice of C_{dl} . The ECSA could be calculated by the following equation

$$\text{ECSA} = \frac{C_{dl}}{C_s} \quad (4)$$

where C_s is the specific capacitance value of a smooth surface of materials under specific electrochemical condition. According to previous study, the value of C_s was 0.04 m F cm⁻² in this calculation.

For OER, the measurements were carried out in O₂ saturated 0.1 M KOH solution with the rotation rate of 1600 rpm at a scan rate of 5 mV s⁻¹. The ohmic potential drop losses of all the electrodes arise from the solution resistance were all corrected (iR-correct) and the solution resistance is determined by the electrochemical impedance spectroscopy (EIS) technique. The EIS was performed within the frequency range

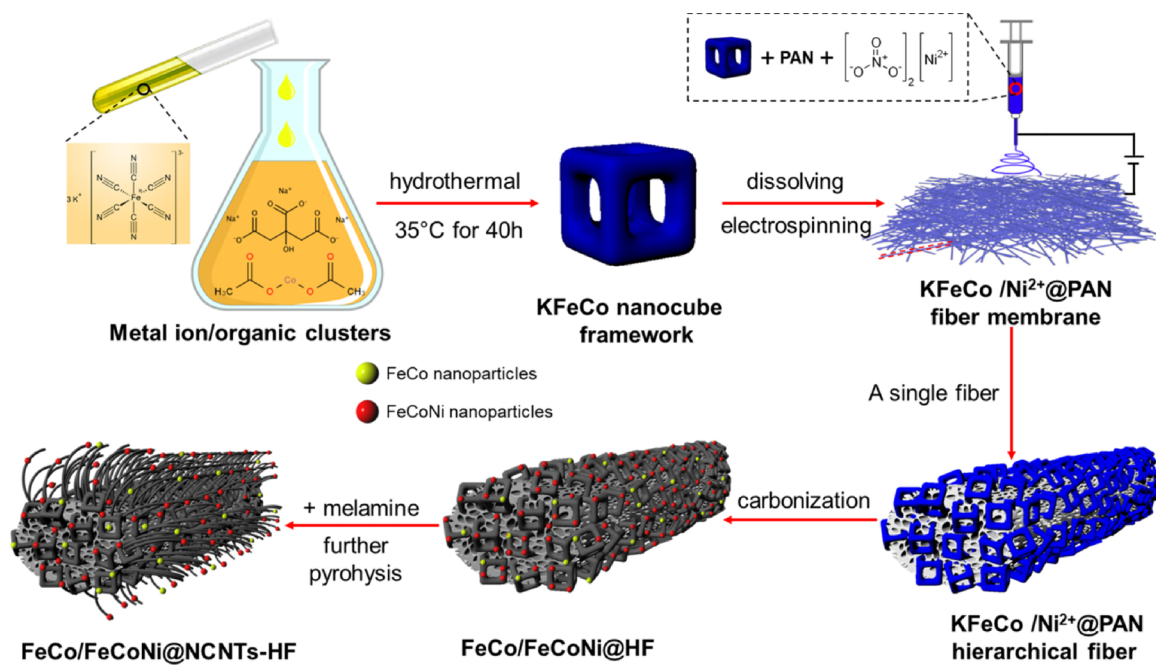
from 0.01 to 10⁵ Hz at 1.60 V (vs. RHE) in 0.1 M KOH. The OER stability was assessed by chronoamperometric measurements at a potential of 1.60 V (vs. RHE).

2.6. Rechargeable Liquid Zn-air battery assembly and measurements

The home-made liquid Zn-air full cells were assembled as shown in Fig. S30. The 6 M KOH + 0.2 M Zn(OAc)₂ mixed solution and polished Zinc foil were used as the electrolyte and anode, respectively. The as-prepared catalysts or mixed commercial Pt/C and RuO₂ (denoted as Pt/C-RuO₂) with a mass ratio of 1:1 coated on carbon paper was used as the air cathode and the effective geometric area that exposed to the electrolyte was about 0.785 cm² (1 cm diameter). The total catalyst loading amount on carbon paper was 2.0 mg cm⁻² for both the as-prepared catalyst and mixed Pt/C-RuO₂. The catalyst ink was prepared as described in the electrochemical measurements. In addition, a flexible self-support air cathode was also prepared by directly coating the homogeneous FeCo/FeCoNi@NCNTs-HF powdered ink onto the flexible self-standing FeCo/FeCoNi@NCNTs-HF membrane, which possesses a mass of 10 mg cm⁻². The loading amount of the FeCo/FeCoNi@NCNTs-HF powdered catalyst on the flexible membrane was 0.5 mg cm⁻². The galvanostatic discharge and charge cycling of the Zn-air batteries was performed through a recurrent galvanostatic pulse method using a Neware battery testing station system (CT-3008) at a current density of 5, and 10 mA cm⁻² with 40 min per cycle (20 min for discharge and 20 min for charge).

3. Results and discussion

The preparation route for FeCo/FeCoNi@NCNTs-HF is schematically depicted in **Scheme 1**. The experimental details are presented in the Experimental section. In brief, KFeCo open nanocube framework is formed by hydrothermal reaction of Co(II)- and Fe(III)-based compounds, and trisodium citrate in aqueous solution [39]. The cubic frameworks are highly uniform with an average size of ~300 nm and constructed by 12 orthogonal edges (Fig. S1). Then a solution of polyacrylonitrile (PAN), KFeCo open nanocube, and nickel (II) nitrate hexahydrate in *N,N*-dimethylformamide (DMF) is electrospun into a blue non-woven fibrous membrane (Fig. S2a). The as-prepared membrane is composed of randomly aligned microfibres that are interconnected to form a network, and each hybrid fibre, with the KFeCo nanocubes uniformly dispersed in the fibre, shows a porous and rough surface structure (Fig. S2b,c). Thereafter, the obtained fibrous membranes undergo the first carbonization in argon gas at a designated temperature (800, 900 or 1000 °C). After the heat treatment process, the fibre morphology is well retained, and FeCo and FeCoNi alloy NPs are uniformly dispersed throughout the porous hybrid fibres (denoted as FeCo/FeCoNi@HF-X, where X indicates the carbonization temperature). The FeCo/FeCoNi@HF-900 is then further pyrolyzed (second pyrolysis) in the presence of melamine at 900 °C for 2 h under nitrogen atmosphere, resulting in FeCo/FeCoNi-decorated CNTs grafted hybrid fibres (FeCo/FeCoNi@NCNTs-HF). During the second pyrolysis stage, melamine serves as the carbon source for the growth of CNTs, which is catalyzed by metallic alloy NPs, and nitrogen source for carbon heteroatom doping [40], while the FeCo and FeCoNi alloy NPs in the porous fibers are partly transformed into the CNTs. The FeCo and FeCoNi NPs, as well as N-doped carbon matrix provide the abundant catalytic active sites and tune the local electronic structure of the hybrid materials, while the CNTs and hierarchical porous framework facilitates electron and mass transfer during the electrocatalytic reactions, respectively. Benefiting from the network structure formed by the electrospun microfibers, the hierarchically porous FeCo/FeCoNi@NCNTs-HF membrane exhibits good flexibility and mechanical robustness, as evidenced by the good integrity of the membrane after 150 bending cycles (Fig. S3).



Scheme 1. Schematic illustration of the preparation process for the FeCo/FeCoNi@NCNTs-HF membrane and its morphology.

As revealed by the field-emission scanning electron microscopy (FESEM) observations (Figs. 1a and S2b,c), the KFeCo nanocube/PAN composite microfibers (KFeCo/Ni²⁺@PAN) are continuous and have abundant pores. After first pyrolysis at 800 or 900 °C, the structural

integrity of the fibres and their network structure are largely retained, while some nanoparticles are formed in the fibres (Figs. 1b, c and S4). Furthermore, the FESEM cross-sectional image (Fig. 1c inset), magnified FESEM images (Fig. S5) and transmission electron microscopy

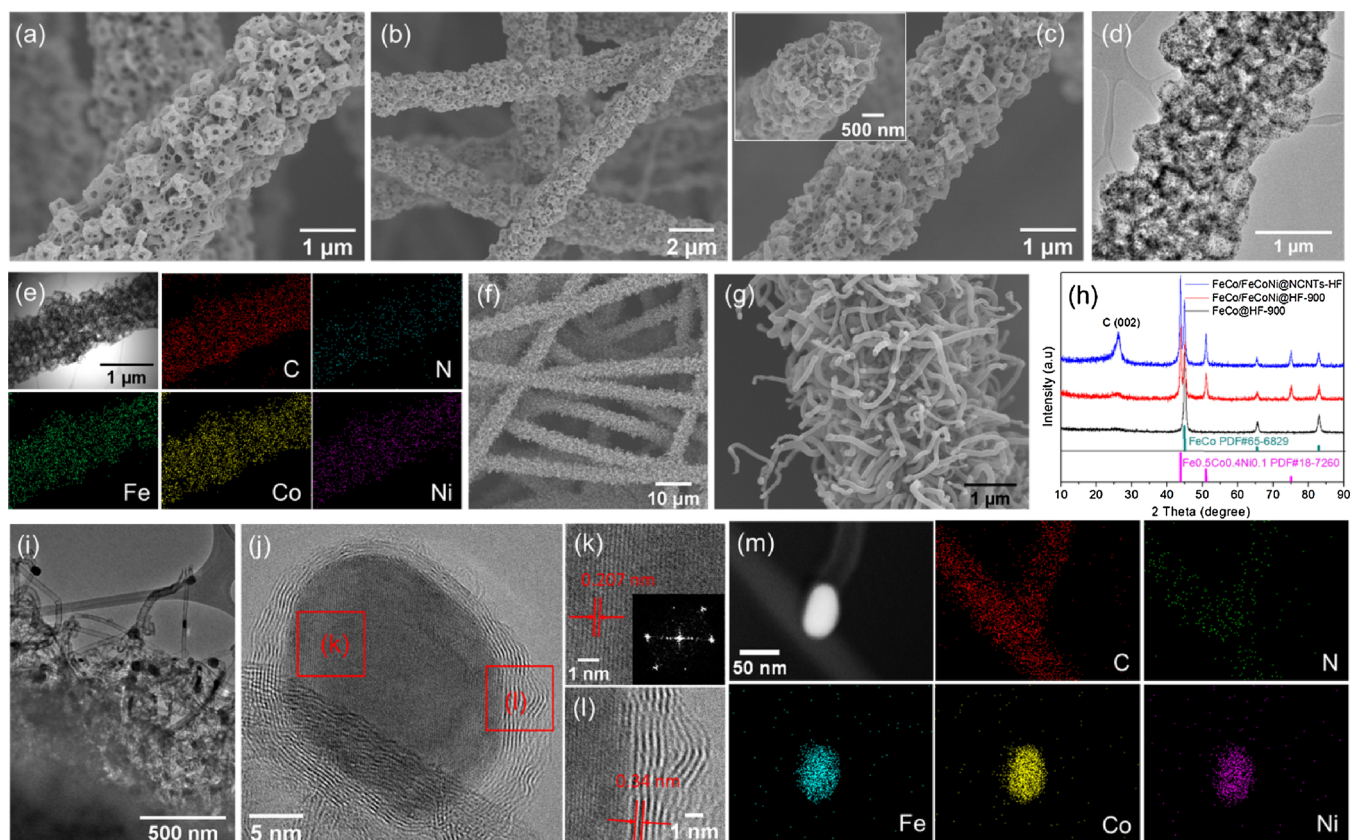


Fig. 1. (a) FESEM image of KFeCo/Ni²⁺@PAN hybrid fibre; (b, c) SEM images, (d) TEM image, and (e) STEM image and corresponding elemental mapping images of FeCo/FeCoNi@HF-900 hybrid fibres; (f, g) SEM images of FeCo/FeCoNi@NCNTs-HF; (h) X-ray diffraction patterns of FeCo@HF-900, FeCo/FeCoNi@HF-900, and FeCo/FeCoNi@NCNTs-HF; (i, j) TEM and HRTEM images, (k, l) Lattice fringe image from the marked area in (j) (the inset is the corresponding FFT pattern), and (m) Dark-field STEM image and corresponding elemental mapping images of FeCo/FeCoNi@NCNTs-HF.

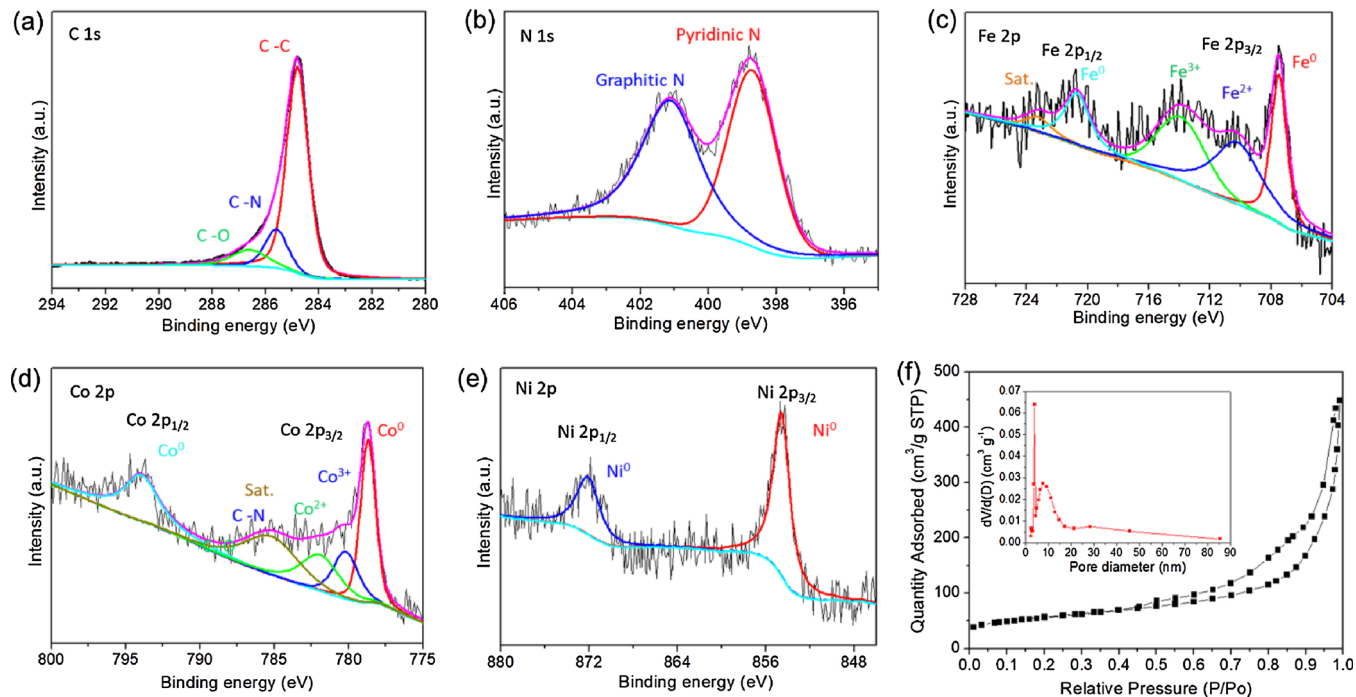


Fig. 2. (a) High-resolution XPS spectra of (a) C 1 s, (b) N 1 s, (c) Fe 2p, (d) Co 2p, (e) Ni 2p core levels for FeCo/FeCoNi@NCNTs-HF; (f) N_2 adsorption-desorption isotherms for FeCo/FeCoNi@NCNTs-HF; the inset is the corresponding pore size distribution.

(TEM) image (Fig. 1d) reveal that these microfibers are composed of numerous open carbon nanocubes that are interconnected with each other by the porous carbon matrix derived from PAN. For comparison, the FeCo@HF-900 with the similar morphology of FeCo/FeCoNi@HF-900 was also prepared (Fig. S6). With further increasing the calcination temperature to 1000 °C, larger nanoparticles are embedded in the obtained FeCo/FeCoNi@HF-1000 carbon fibres with the open carbon nanocubes and nanopores partially collapsed (Fig. S7). From the magnified TEM images (Fig. S8), we can see that the metal-based nanoparticles with an average diameter of ~16 nm are uniformly distributed within the open nanocube edges and porous carbon matrix. The high-resolution transmission electron microscope (HRTEM) image (Fig. S9), further shows that the alloy particles are surrounded by several graphene layers with interplanar spacing of 0.34 nm [41]. The scanning transition electron microscopy (STEM) and corresponding energy-dispersive X-ray (EDX) elemental mapping images (Figs. 1e and S10) also confirm that the C, N, Fe, Co, and Ni elements are homogeneously distributed in the entire porous carbon matrix for FeCo/FeCoNi@HF-900. After the second pyrolysis, the resultant FeCo/FeCoNi@NCNTs-HF has a large number of CNTs with the lengths of several hundred nanometers and average diameters of ~32 nm warped on the hybrid carbon fibres (Fig. 1f,g). The presence of CNTs creates a hierarchical interconnected network, which could promote the diffusion of electrolyte and the transport of oxygen in the membranes. For comparison, the FeCo@NCNTs-HF with the similar morphology of FeCo/FeCoNi@NCNTs-HF was also prepared (Fig. S11).

The structural features of FeCo/FeCoNi@NCNTs-HF and reference samples were studied by X-ray diffraction (XRD) technique. As shown in Fig. 1h, the XRD pattern of the FeCo@HF-900, which was prepared using the same procedure as that for FeCo/FeCoNi@HF-900 but without the addition of Ni^{2+} , reveals that the dominant phase of the hybrid is bimetal FeCo alloy with diffraction peaks centered at 44.9°, 65.4°, and 82.9°, which can be ascribed to the (100), (200), and (211) facets of FeCo alloy (JCPDS No. 65-6829) [20,42]. By contrast, the FeCo/FeCoNi@HF-900 exhibits three new distinctive peaks located at 43.8°, 51.0°, and 75.0°, corresponding to the (111), (200), and (220) facets of $Fe_{0.5}Co_{0.4}Ni_{0.1}$ alloy (JCPDS No. 18-7260). Furthermore, the

relatively broad weak diffraction peak at 26.2° can be assigned to the (002) lattice planes of graphitic carbon (JCPDS No. 41-1487) [43]. With increasing the pyrolysis temperature, this peak becomes stronger, indicating the generation of an increasingly ordered graphitic structure (Fig. S12). The FeCo/FeCoNi@NCNTs-HF shows a similar XRD pattern to that of FeCo/FeCoNi@HF-900, indicating that the FeCoNi alloy is the dominant phase, while the peak intensity at 26.2° is significantly increased due to the presence of highly graphitized carbon walls in CNTs (Fig. S13). This can be confirmed by the lower ratio of integrated intensities of the D band (located at 1345 cm^{-1}) to G band (located at 1590 cm^{-1}) (I_D/I_G) in the Raman spectra (Fig. S14).

The microstructure of FeCo/FeCoNi@NCNTs-HF is further investigated by TEM (Figs. 1i and S15). It can be observed that the CNTs-grafted carbon fibre possesses a kinetically favourable open structure, in which the alloy nanoparticles with an average size of ~16.6 nm are homogeneously embedded in the carbon matrix, especially at the tip of the CNTs. The HRTEM image in Fig. 1j shows a typical alloy NP with the lattice spacing of 0.207 nm (Fig. 1k), according to the corresponding FFT pattern (Fig. 1k inset), which corresponds to the (111) plane of the $Fe_{0.5}Co_{0.4}Ni_{0.1}$ alloy. This NP is encapsulated by a few-layered carbon shell with interplanar spacing of 0.34 nm (Fig. 1l). Meanwhile, alloy NPs with the lattice spacing of 0.201 nm, corresponding to the (110) plane of the FeCo alloy, are also observed being anchored on the FeCo/FeCoNi@NCNTs-HF (Fig. S16) [20]. Such CNT-supported alloy NPs covered with thin graphene shells could promote the catalytic process, enhance the conductivity, and also benefit the catalytic stability. The dark-field STEM and corresponding EDX elemental mapping analysis also clearly reveals that the uniform distribution of C, N, Fe, Co, and Ni elements in the CNTs-grafted hybrid fibre membrane, and Fe, Co, Ni elements and Fe, Co elements are evenly distributed in the carbon-coated FeCoNi and FeCo alloy NPs, respectively (Figs. S17, 1 m and S18). Fig. S19 displays the thermogravimetric analysis (TGA) curves of the FeCo/FeCoNi@NCNTs-HF. The weight loss occurring before ~500 °C is due to the removal of porous carbon and graphitic layers in air flow, while the subsequent slight weight increase was related to the oxidation of metallic FeCo, and FeCoNi NPs [44]. The total amount of FeCo and FeCoNi alloys were

measured to be about 38.8 wt%, which was in good agreement with the EDX result (Fig. S20).

The surface chemical composition of the FeCo/FeCoNi@NCNTs-HF and reference materials were further investigated by X-ray photoelectron spectroscopy (XPS). The XPS full survey spectrum confirms the presence of C, N, O, Fe, Co, and Ni (Fig. S21a). The total Fe, Co and Ni contents measured from XPS are much lower than those obtained from the EDX result (Figs. S21b and S20), confirming that part of Fe, Co, and Ni species are embedded in the porous carbon matrix. High-resolution C 1 s spectrum (Fig. 2a) reveals the presence of C–C (284.8 eV), C–N (285.6 eV), and C=O (286.6 eV) [45,46]. The high-resolution N 1s can be divided into two characteristic peaks at 398.7, and 401.2 eV, which are assigned to pyridinic-N, and graphitic-N, respectively (Fig. 2b) [42,47]. It is believed that pyridinic-N can act as the active component to enhance the electron-donating capability, and the abundant pyridinic-N can also coordinate with metal atoms to optimize the local electronic structure as well as improve electrical conductivity and surface wettability, which should be beneficial for the electrochemical processes [5,42,48]. Meanwhile, previous reports indicated that graphitic-N species could also service as active sites for ORR and OER, especially boost the limiting current density [49,50]. As shown in Fig. S22, FeCo/FeCoNi@NCNTs-HF possesses the highest N content, including pyridinic-N and graphitic-N, among the as-prepared samples. Fig. 2c shows two bands at 707.5 and 720.7 eV in the high-resolution spectrum of Fe 2p, which correspond to zero-valence state Fe, indicate metallic iron in FeCo and FeCoNi alloys [22,48]. The relatively weak bands centred at 710.2 and 714.0 eV can be assigned to Fe^{2+} and Fe^{3+} species, respectively, while a small component of the Fe 2p band located at 723.2 eV is attributed to the satellites [20]. Additionally, Fig. 2d presents the zero-valence state Co (778.7 and 793.9 eV) in Co 2p

spectra, indicating the existence of metallic cobalt in FeCo and FeCoNi alloys [20]. Ionic state Co^{3+} (780.2 eV) and Co^{2+} (782.0 eV) with shakeup satellites (785.2 eV) were also observed [51]. The high-resolution Ni 2p spectra can be divided into two bands located at 854.6 and 872.1 eV (Fig. 2e), respectively, which can be assigned as the subpeak of metallic nickel in FeCoNi alloys [52]. These results indicate the successful introduction of FeCo and FeCoNi metallic alloy NPs into N-doped carbon of the hybrid fibrous membrane.

The N_2 adsorption-desorption of the FeCo/FeCoNi@NCNTs-HF catalyst (Fig. 2f) shows a typical type IV isotherm with a distinct hysteresis loop, suggesting the presence of abundant mesoporous pores [40]. Moreover, the pore-size distribution curve (Fig. 2f inset) derived from the N_2 desorption indicates that a large number of nanopores are in the range of 2–20 nm, confirming that mesoporous structure is dominant. The porous FeCo/FeCoNi@NCNTs-HF displays a high Brunauer-Emmett-Teller (BET) surface area of $211.7 \text{ cm}^2 \text{ g}^{-1}$ and a Barrett-Joyner-Halenda (BJH) pore volume of $0.687 \text{ cm}^3 \text{ g}^{-1}$. The unique hierarchical porous feature and high porosity endow the hybrid catalyst more catalytically active sites and are also beneficial for the charge and mass transport during the electrochemical reactions.

The electrocatalytic ORR performance of the as-prepared catalysts and commercial Pt/C were investigated in a 0.10 M KOH solution using a typical three-electrode system at room temperature. The cyclic voltammetry (CV) curves of the FeCo/FeCoNi@NCNTs-HF are shown in Fig. 3a. No obvious redox peak can be observed in the N_2 -saturated electrolyte while there is a distinct peak at 0.834 V in O_2 -saturated electrolyte, suggesting a high catalytic activity toward ORR, which is comparable to that of commercial Pt/C catalyst (0.856 V). Furthermore, the oxygen reduction peak is more positive than that of FeCo/FeCoNi@HF-800 (0.775 V), FeCo/FeCoNi@HF-900 (0.799 V), FeCo/FeCoNi@

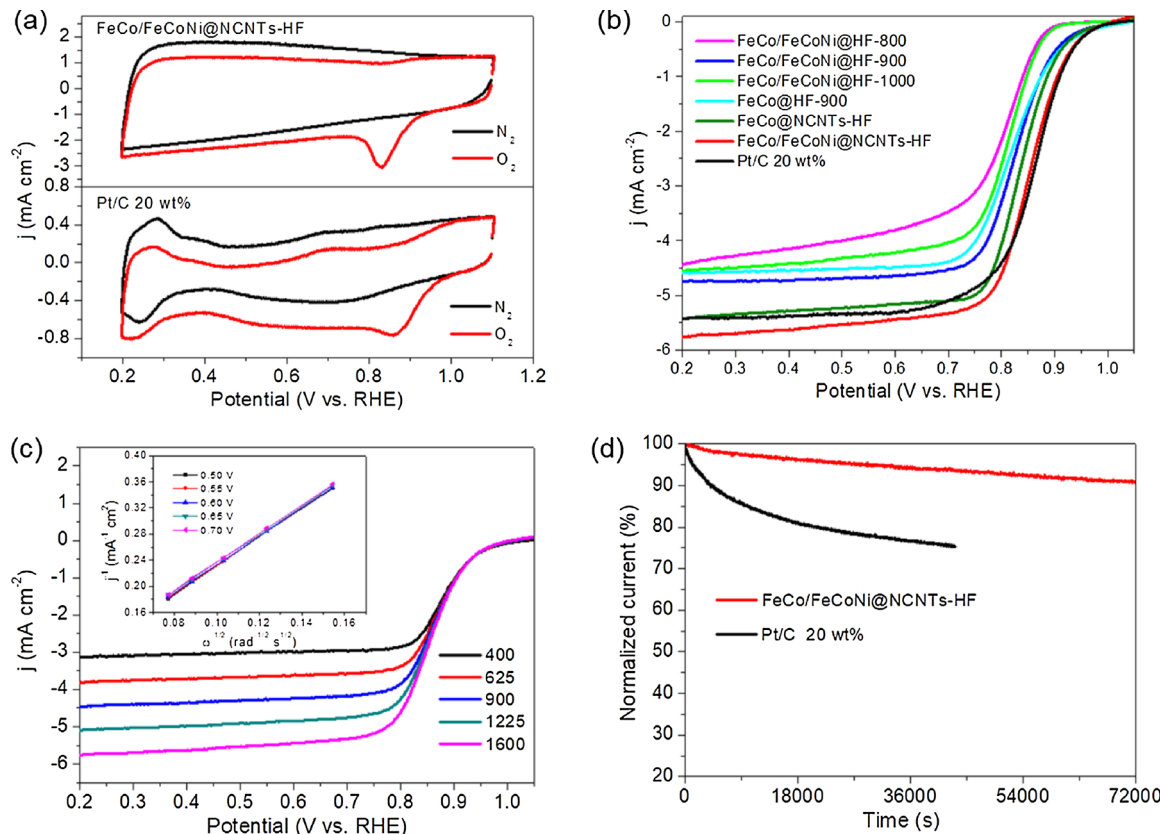


Fig. 3. Electrocatalytic ORR activities: (a) CV curves of FeCo/FeCoNi@NCNTs-HF and Pt/C in N_2 - and O_2 -saturated 0.1 M KOH electrolyte at scan rate of 50 mV s^{-1} ; (b) LSV curves of FeCo/FeCoNi@HF-800, FeCo/FeCoNi@HF-900, FeCo/FeCoNi@HF-1000, FeCo@HF-900, FeCo@NCNTs-HF, FeCo/FeCoNi@NCNTs-HF and Pt/C catalysts in O_2 -saturated 0.1 M KOH electrolyte at scan rate of 5 mV s^{-1} at 1600 rpm; (c) LSV curves of FeCo/FeCoNi@NCNTs-HF at various rotating speeds, inset: the corresponding K-L plots at different potentials; (d) ORR chronoamperometric response of FeCo/FeCoNi@NCNTs-HF and Pt/C at a constant potential of 0.80 V (vs. RHE).

HF-1000 (0.785 V), FeCo@HF-900 (0.794 V), and FeCo@NCNTs-HF (0.815 V), as shown in Fig. S23, highlighting the superior ORR catalytic activity of the former.

Linear sweep voltammetry (LSV) measurements on a rotating disk electrode (RDE) were further performed to evaluate the ORR activity of the samples as well as the commercial Pt/C catalyst (Fig. 3b). The FeCo/FeCoNi@NCNTs-HF catalyst possesses a high half-wave potential ($E_{1/2} = 0.850$ V vs. RHE), which is comparable to that of Pt/C catalyst ($E_{1/2} = 0.861$ V) and much more positive than that of other control samples. In particular, the FeCo/FeCoNi@NCNTs-HF catalyst also exhibits the largest limited current density (-5.775 mA cm⁻²) at 0.20 V (vs. RHE), indicating the advantage of its unique hierarchical porous structure, which facilitates gas diffusion and mass transfer. Furthermore, FeCo/FeCoNi@NCNTs-HF possesses a kinetic current density (J_k) of 23.09 mA cm⁻² at 0.80 V, which is slightly smaller than that of Pt/C (23.75 mA cm⁻²) and much larger than that of the as-prepared reference samples (Fig. S24). By contrast, the FeCo/FeCoNi@HF-800 shows the lowest activity with a half-wave potential of ~ 0.797 V, which may be due to the relative low conductivity caused by insufficient carbonization. The half-wave potential for FeCo/FeCoNi@HF-900 ($E_{1/2} = 0.826$ V) is higher than the one observed for the catalyst prepared at 1000 °C ($E_{1/2} = 0.811$ V), indicating the crucial influence of N-doping content on the ORR activity (Fig. S22). Furthermore, compared with FeCo@HF-900 ($E_{1/2} = 0.820$ V), the half-wave potential of FeCo@NCNTs-HF shows an obvious increase ($E_{1/2} = 0.835$ V). Meanwhile, FeCo/FeCoNi@NCNTs-HF also exhibits a significantly positive half-wave potential and large limit current density in comparison to that of FeCo/FeCoNi@HF-900, suggesting the introduction of CNTs and high N-doping content contribute to the enhancement of ORR activity. It can thus be concluded that the hierarchical porous structure, interplay of metallic alloys and nitrogen species, as well as the good conductivity all positively influence the ORR performance.

The ORR kinetics and reaction pathways of the FeCo/FeCoNi@NCNTs-HF catalysts were evaluated by LSV measurements at various rotation speeds ranging from 400 to 1600 rpm. As shown in Figs. 3c and S25, the diffusion-limited current densities increase with increasing the rotation speed due to the shortened O₂ diffusion distance in the electrolyte at higher rotation speeds. More importantly, based on the LSV results, the corresponding Koutecky-Lecich (K-L) plots were also obtained to investigate the electron transfer kinetics of the ORR process for FeCo/FeCoNi@NCNTs-HF (Fig. 3c inset). The K-L plots of FeCo/FeCoNi@NCNTs-HF exhibit good linearity at different potentials, implying first-order reaction kinetics with respect to the dissolved oxygen concentration. Meanwhile, the calculated electron-transfer number derived from the slopes of the K-L plots is in the range of 3.98–4.00, which is almost the same as that of the commercial Pt/C catalyst (3.99–4.00) (Fig. S25), demonstrating a predominant four-electron transfer process of FeCo/FeCoNi@NCNTs-HF toward ORR. By contrast, the electron transfer numbers for FeCo/FeCoNi@HF-800, FeCo/FeCoNi@HF-900, FeCo/FeCoNi@HF-1000, and FeCo@HF-900 are only 3.28–3.61, 3.92–3.95, 3.48–3.62, and 3.90–3.94, respectively (Fig. S25). Furthermore, the approximate Tafel slopes of FeCo/FeCoNi@NCNTs-HF (71 mV decade⁻¹) and Pt/C catalyst (69 mV decade⁻¹) further suggest a quick charge and mass transfer on these catalysts (Fig. S26). The electrochemical active surface area (ECSA), which is an important indicator to inherently determine the electrocatalytic activity, was also obtained. The ECSA related to the double-layer capacitances was calculated by measuring the CV curves with various scan rates from 5 to 60 mV s⁻¹ (Fig. S27). The double-layer capacitance of FeCo/FeCoNi@NCNTs-HF was measured to be 27.14 mF cm⁻² (Fig. S27), which is significantly higher than that of the FeCo/FeCoNi@HF-900 (14.54 mF cm⁻²), implying that the formation of CNTs on porous carbon matrix and the introduction of nitrogen dopants could increase the ECSA for exposing more active sites. Besides, FeCo/FeCoNi@NCNTs-HF also exhibits a larger double-layer capacitance compared with FeCo@NCNTs-HF (19.24 mF cm⁻²), which reveals the advantage of the

introduction of FeCoNi alloys in improving ECSA. Therefore, the high catalytic activity of the hierarchically porous FeCo/FeCoNi@NCNTs-HF is associated with the highly accessible active sites as a result of the large ECSA. Besides the catalytic activity, the durability of FeCo/FeCoNi@NCNTs-HF, which is also an important parameter for the practical application of the catalyst, is also evaluated by chronoamperometric measurement in O₂-saturated 0.1 M KOH solution. As presented in Fig. 3d, about 90.7% of the original current was maintained for the FeCo/FeCoNi@NCNTs-HF after 72000 s (15 h) of continuous operation, while the commercial Pt/C catalyst suffered from a much higher degree of degradation with only $\sim 71.2\%$ retention after 43200 s (12 h), indicating the superior durability of the FeCo/FeCoNi@NCNTs-HF over the commercial Pt/C catalyst. The outstanding durability of FeCo/FeCoNi@NCNTs-HF can be attributed to its robust carbon-based hierarchically porous architecture and the formation of multiple graphene layers to wrap and protect the alloy activity sites.

To demonstrate the bifunctional oxygen catalytic activity, the electrocatalytic OER performances of the samples were further investigated in O₂-saturated 0.1 M KOH electrolyte at the scan rate of 5 mV s⁻¹. As shown in Fig. 4a, the FeCo/FeCoNi@NCNTs-HF shows a current density of 10 mA cm⁻² at the potential ($E_{j=10}$) of 1.608 V (vs RHE), which is much lower than those of the control samples, and is slightly higher than that of the commercial RuO₂ catalyst ($E_{j=10} = 1.601$ V), demonstrating its superior electrocatalytic activity toward OER. Furthermore, the FeCo/FeCoNi@NCNTs-HF also exhibits the largest OER current density and the fastest current-density rising in the whole potential window among all the catalysts tested, further revealing the outstanding OER catalytic activity of FeCo/FeCoNi@NCNTs-HF. It is worth mentioning that the OER potential of FeCo/FeCoNi@HF-900 at 10 mA cm⁻² is only 1.628 V, which is 68 mV smaller than that of FeCo@HF-900. Since they have similar morphology and N-doping content (Fig. S22), the introduction of FeCoNi alloys contribute significantly to OER activity enhancement. Moreover, FeCo/FeCoNi@NCNTs-HF also exhibits an obvious lower potential at the current density of 10 mA cm⁻² in comparison to that of FeCo@NCNTs-HF ($E_{j=10} = 1.680$ V), further confirming the key role of FeCoNi alloys for the enhancement of OER activity. Furthermore, FeCo/FeCoNi@NCNTs-HF has the smallest charge transfer resistance among the as-prepared electrodes, as shown by their electrochemical impedance spectroscopy (EIS) (Fig. S28), highlighting that the enhanced electronic conductivity plays an important role in enhancing the OER activity. In addition, the catalytic kinetics of the above catalysts for OER was also estimated by the Tafel plots (Fig. 4b). The lower Tafel slope of FeCo/FeCoNi@NCNTs-HF (66 mV dec⁻¹) in comparison with FeCo/FeCoNi@HF-800 (104 mV dec⁻¹), FeCo/FeCoNi@HF-900 (86 mV dec⁻¹), FeCo/FeCoNi@HF-1000 (88 mV dec⁻¹), FeCo@HF-900 (142 mV dec⁻¹), and FeCo@NCNTs-HF (118 mV dec⁻¹), further confirms its optimized OER kinetics. Furthermore, the durability of the FeCo/FeCoNi@NCNTs-HF for the OER was assessed by chronoamperometry in 0.1 M KOH at the potential of 1.60 V. As shown in Fig. 4c, FeCo/FeCoNi@NCNTs-HF exhibits good stability with about 76.5% current retention after 45000 s (12.5 h) continuous reactions and the core-shell structure (alloys coated by graphene layers) was well maintained (Fig. S29). By contrast, the current retention of commercial RuO₂ is only 40% after 36000 s (10 h) under the same conditions. These results indicate FeCo/FeCoNi@NCNTs-HF possesses superior electrochemical durability towards OER in alkaline medium. To further demonstrate the bifunctional activities of the catalysts, the difference between the overpotential at an OER current density of 10 mA cm⁻² and ORR half-wave overpotential ($\Delta E = E_{j=10} - E_{\text{half-wave}}$) was also measured. As shown in Fig. 4d, the ΔE value obtained for the FeCo/FeCoNi@NCNTs-HF is 0.758 V, which is considerably smaller than the ones from the control samples. Moreover, the overvoltage gap of FeCo/FeCoNi@NCNTs-HF is comparable and even lower than that of previously reported advanced bifunctional catalysts, as shown in Table S1, demonstrating the superiority of FeCo/FeCoNi@NCNTs-HF in bifunctional catalysis.

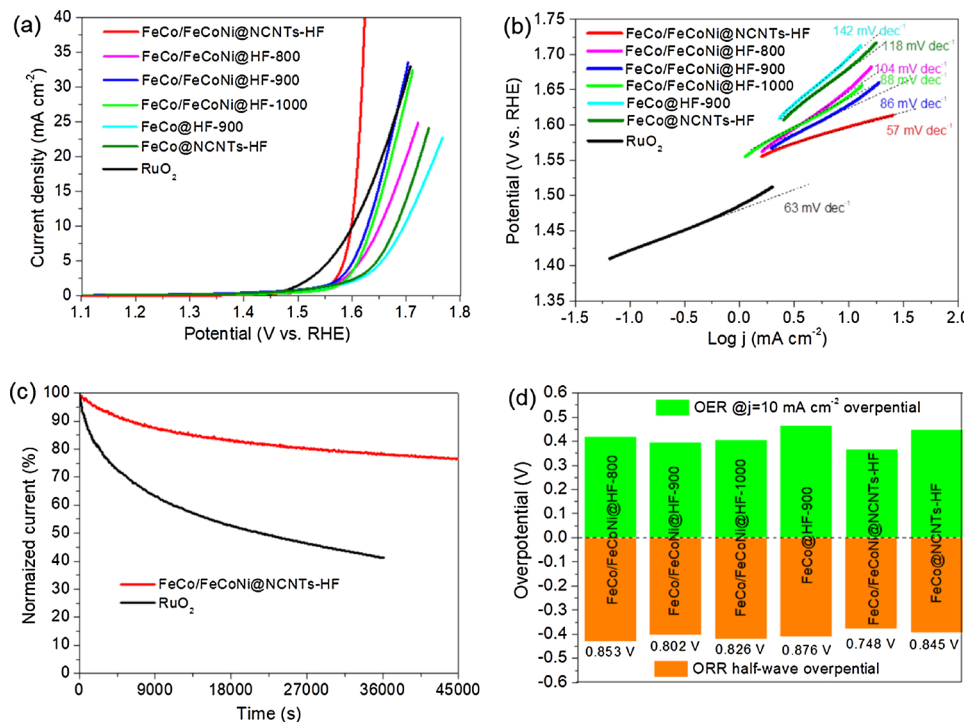


Fig. 4. Electrocatalytic OER activities: (a) LSV curves of FeCo/FeCoNi@HF-800, FeCo/FeCoNi@HF-900, FeCo/FeCoNi@HF-1000, FeCo@HF-900, FeCo@NCNTs-HF, FeCo/FeCoNi@NCNTs-HF and RuO₂ catalysts in 0.1 M KOH electrolyte at scan rate of 5 mV s⁻¹ at 1600 rpm; (b) Tafel plots obtained from the corresponding LSV curves; (c) OER chronoamperometric response of FeCo/FeCoNi@NCNTs-HF and RuO₂ at a constant potential of 1.60 V (vs. RHE). (d) Potential difference between the E_{half-wave} of ORR and E_{j=10} of FeCo/FeCoNi@NCNTs-HF and other reference catalyst.

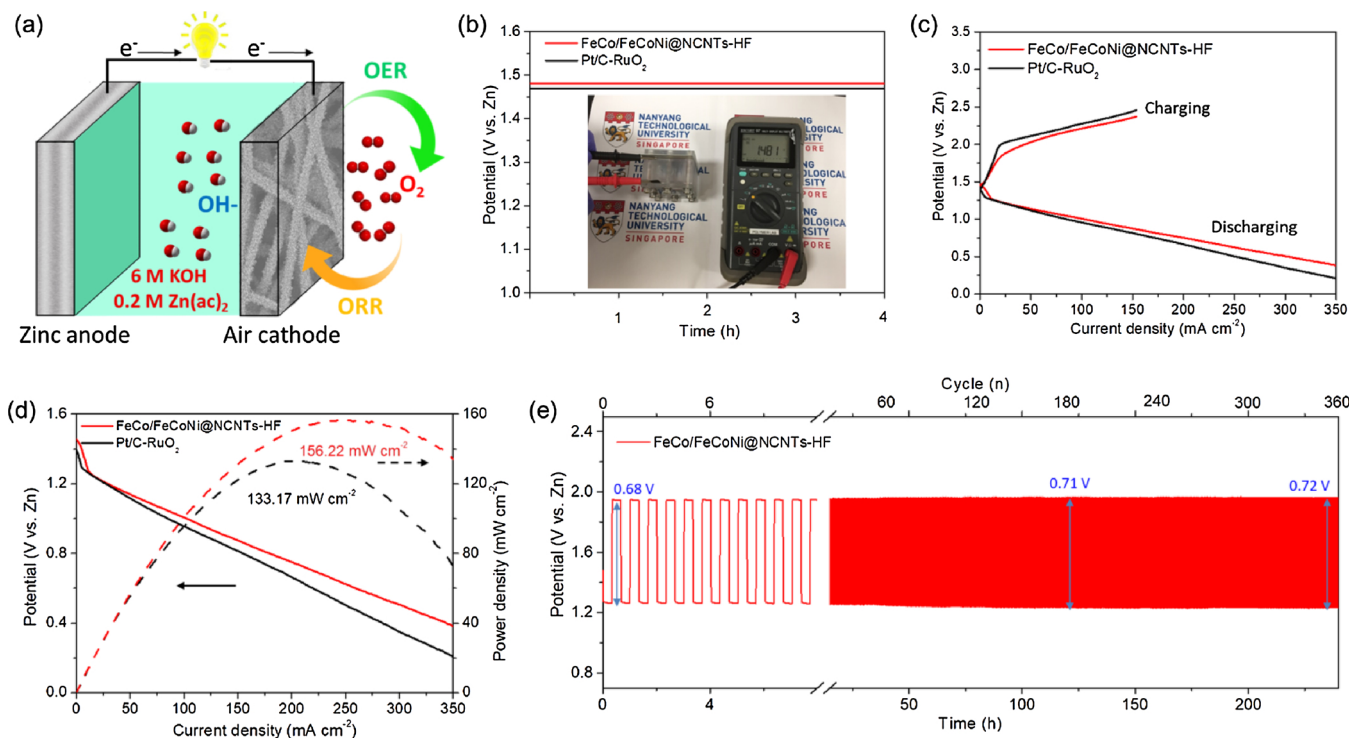


Fig. 5. (a) Schematic illustration of the liquid Zn-air battery configuration; (b) Open circuit plots of the Zn-air battery with FeCo/FeCoNi@NCNTs-HF and Pt/C-RuO₂ serving as the air cathode, respectively; inset: the corresponding photograph of the Zn-air battery equipped with FeCo/FeCoNi@NCNTs-HF catalyst with an open-circuit voltage of 1.481 V; (c) Charge and discharge polarization curves, (d) discharge polarization curves and the corresponding power density plots of the Zn-air battery with FeCo/FeCoNi@NCNTs-HF and Pt/C-RuO₂ catalysts; (e) Galvanostatic cycling stability of Zn-air battery with FeCo/FeCoNi@NCNTs-HF catalyst at a current density of 5 mA cm⁻².

The outstanding ORR and OER performance makes FeCo/FeCoNi@NCNTs-HF a promising material to serve as the bifunctional catalyst for reversible oxygen reactions in air cathodes of metal-air batteries. To demonstrate the practical applicability, as illustrated in Figs. 5a and S30, two electrodes rechargeable Zn-air batteries were assembled using the metallic Zn plate as the anode. FeCo/FeCoNi@NCNTs-HF as well as

mixed commercial Pt/C/RuO₂ catalysts with equal ratios (denote as Pt/C-RuO₂) loaded on carbon paper were used as the air cathode, respectively, with an aqueous solution of 6 M KOH and 0.2 M Zn(ac)₂ as the electrolyte. The open-circuit potential of the battery employing FeCo/FeCoNi@NCNTs-HF as the air cathode catalyst was 1.481 V (Fig. 5b and inset), which is higher than that of the Pt/C-RuO₂ air

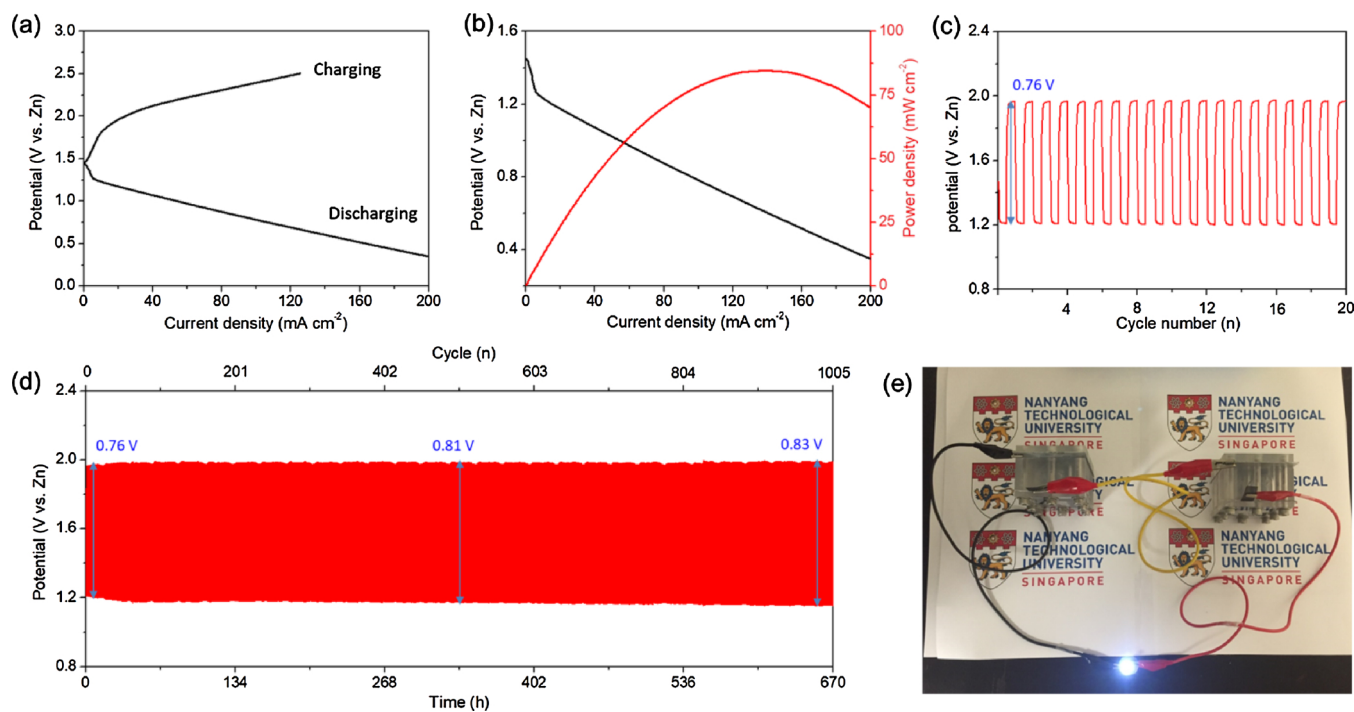


Fig. 6. (a) Charge and discharge polarization curves, (b) discharge polarization curves and the corresponding power density plots of the Zn-air battery with the self-supported FeCo/FeCoNi@NCNTs-HF air cathode; (c) and (d) Galvanostatic cycling stability of Zn-air battery with the self-supported FeCo/FeCoNi@NCNTs-HF air cathode at a current density of 5 mA cm⁻²; (e) Photograph of a LED (~3.0 V) powered by two Zn-air batteries in series that are based on the self-supported FeCo/FeCoNi@NCNTs-HF air cathode.

cathode (1.469 V). As presented in Fig. 5c, the charge and discharge polarization curves suggest that the battery based-on FeCo/FeCoNi@NCNTs-HF demonstrates more ideal charge and discharge curves than the Pt/C-RuO₂ reference, especially at relatively high current densities. The smaller voltage gap between the ORR and OER curves of FeCo/FeCoNi@NCNTs-HF can be attributed to the hierarchically porous structures and large specific surface area of N-doped CNTs as the support for FeCo and FeCoNi alloys, which benefit the diffusion of oxygen species and electrolytes to the actives sites, and provide increasing amount of active sites, respectively. Fig. 5d displays the discharge polarization curves and the corresponding power density plots. The maximum power density of the Zn-air battery equipped with FeCo/FeCoNi@NCNTs-HF catalyst is calculated to be as high as 156.22 mW cm⁻², which is higher than that with Pt/C-RuO₂ catalyst (133.17 mW cm⁻²). After a long-term galvanostatic discharge at 5 and 10 mA cm⁻² for 50 h, no significant voltage drop is observed (Fig. S31), indicating the excellent catalytic stability for ORR in the Zn-air battery. Meanwhile, there is a large gravimetric specific capacity for FeCo/FeCoNi@NCNTs-HF (783 mAg g⁻¹) at a discharge current of 5 mA cm⁻² (normalized to the mass of consumed Zn, Fig. S32a). Moreover, FeCo/FeCoNi@NCNTs-HF generates a specific capacity of 762 mA h g⁻¹ at the current density of 10 mA cm⁻², outperforming that of the Pt/C-RuO₂ air cathode (735 mA h g⁻¹, Fig. S32b).

The long-term rechargeability of FeCo/FeCoNi@NCNTs-HF for Zn-air battery was also evaluated by galvanostatic charge-discharge (40 min per-cycle, with 20 min discharge and 20 min charge). As demonstrated in Fig. 5e, FeCo/FeCoNi@NCNTs-HF provides a narrow charge-discharge gap of 0.68 V at a constant current density of 5 mA cm⁻², and excellent durability without noticeable voltage fading over 240 h (360 cycles). Furthermore, the FeCo/FeCoNi@NCNTs-HF also exhibits a small voltage gap (0.75 V) and good stability at the current density of 10 mA cm⁻², with no obvious voltage change over 120 h (180 cycles) (Fig. S33a), while the Zn-air battery based on Pt/C-RuO₂ shows limited cyclability of less than 60 h (90 cycles) (Fig. S33b). The excellent cycling stability of FeCo/FeCoNi@NCNTs-HF can be

attributed to its robust hybrid structure, where active alloy NPs stitched in the graphitized carbon support, providing enhanced stability. As shown in Table S2, The performance of our Zn-air battery is comparable and even better than most advanced rechargeable Zn-air batteries with carbon-based nanomaterials as the electrocatalysts reported so far.

The test results presented above were obtained from the batteries where FeCo/FeCoNi@NCNTs-HF powder was used as the electrocatalyst in the air cathode. Encouraged by the good flexibility and mechanical robustness of the FeCo/FeCoNi@NCNTs-HF membrane, we further explored the use of FeCo/FeCoNi@NCNTs-HF membrane as self-supported air cathode in a liquid rechargeable Zn-air battery. The electrode was prepared by loading few amount of FeCo/FeCoNi@NCNTs-HF catalyst ink onto the flexible FeCo/FeCoNi@NCNTs-HF membrane (for detail see the Experimental section). Fig. 6a shows the discharge and charge polarization curves of the Zn-air battery based on this flexible, self-supported FeCo/FeCoNi@NCNTs-HF air cathode. Fig. 6b depicts the polarization and corresponding power density plots, from which the peak power density was calculated as 84.6 mW cm⁻² at 139 mA cm⁻². The cycling stability (40 min per-cycle, with 20 min discharge and 20 min charge) of the liquid Zn-air battery based on self-supported FeCo/FeCoNi@NCNTs-HF was first measured at the current density of 5 mA cm⁻². The initial charge and discharge potentials of the Zn-air cell were 1.21 V and 1.97 V with a small voltage gap of 0.76 V (Fig. 6c). The excellent rechargeability was further demonstrated by 670 h (1005 cycles) long-term cycling test without obvious deterioration for the voltage gap (Fig. 6d), which is superior to most of the previous reported Zn-air battery (Table S2). Particularly, the battery using self-supported FeCo/FeCoNi@NCNTs-HF air cathode is also capable of withstanding a current density of 10 mA cm⁻², delivering a voltage gap of 0.86 V for 140 h (210 cycles) (Fig. S34). As exemplified in Fig. S35, one Zn-air cell based on self-supported FeCo/FeCoNi@NCNTs-HF air cathode can generate an open-circuit potential of 1.453 V. Moreover, the light-emitting diodes (LED) could be powered by two such Zn-air cells in series (Fig. 6e and Video 1), further demonstrating its promise for practical applications in Zn-air batteries.

4. Conclusion

In summary, a novel synthetic strategy for the preparation of FeCo/FeCoNi/N-doped CNTs-grafted porous polyhedron-derived robust fiber membranes is successfully demonstrated. The hybrid fiber exhibits remarkable bifunctional electrocatalytic activity and stability toward both ORR and OER, which are competitive to commercial Pt/C and RuO₂ electrocatalysts for ORR and OER, respectively. The excellent electrocatalytic performance can be ascribed to the following compositional and morphological features: (i) the graphene layers covered FeCo, FeCoNi alloys and active N-doped carbon phase, as well as the synergy among these components generate abundant active electrolytic sites; (ii) the combination of FeCo, FeCoNi alloys and N-doped CNTs-grafted carbon matrix alter the surface electron configuration, which contributing to oxygen adsorption/activation and efficient electron transfer; (iii) the interconnected 3D hierarchical porous structure and high specific surface area enable the effective exposure of more active sites, as well as fast mass transfer and intimate contact between the electrolyte and active materials during the reactions. Furthermore, when worked as a bifunctional catalyst in a Zn-air battery, the hybrid catalysts shows gratifying power density, large specific capacity, and exceptional cycle stability. This work will pave the way to design advanced bifunctional catalysts for the development of cost-effective, highly efficient and durable energy conversion and storage devices.

Acknowledgement

This work was supported by the Agency for Science, Technology and Research and Nanyang Technological University, Singapore for providing funding and PhD scholarships.

Appendix A. Supplementary data

Supplementary material related to this article can be found, in the online version, at doi:<https://doi.org/10.1016/j.apcatb.2019.04.027>.

References

- [1] X. Liu, L. Dai, Carbon-based metal-free catalysts, *Nat. Rev. Mater.* 1 (2016) 16064.
- [2] J. Fu, Z.P. Cano, M.G. Park, A. Yu, M. Fowler, Z. Chen, Electrically rechargeable zinc-air batteries: progress, challenges, and perspectives, *Adv. Mater.* 29 (2017) 1604685.
- [3] Y. Li, H. Dai, Recent advances in zinc-air batteries, *Chem. Soc. Rev.* 43 (2014) 5257–5275.
- [4] Z.W. Seh, J. Kibsgaard, C.F. Dickens, I. Chorkendorff, J.K. Norskov, T.F. Jaramillo, Combining theory and experiment in electrocatalysis: insights into materials design, *Science* 355 (2017) 6321.
- [5] B.Y. Xia, Y. Yan, N. Li, H.B. Wu, X.W. Lou, X. Wang, A metal–organic framework-derived bifunctional oxygen electrocatalyst, *Nat. Energy* 1 (2016) 15006.
- [6] J. Fu, F.M. Hassan, C. Zhong, J. Lu, H. Liu, A. Yu, Z. Chen, Defect engineering of halogen-tailored oxygen electrocatalysts for rechargeable quasi-solid-state zinc-air batteries, *Adv. Mater.* 29 (2017) 1702526.
- [7] J. Zhang, Z. Zhao, Z. Xia, L. Dai, A metal-free bifunctional electrocatalyst for oxygen reduction and oxygen evolution reactions, *Nat. Nanotechnol.* 10 (2015) 444.
- [8] X.R. Wang, J.Y. Liu, Z.W. Liu, W.C. Wang, J. Luo, X.P. Han, X.W. Du, S.Z. Qiao, J. Yang, Identifying the key role of Pyridinic-N-Co bonding in synergistic electrocatalysis for reversible ORR/OER, *Adv. Mater.* 30 (2018) 1800005.
- [9] G. Fu, J. Wang, Y. Chen, Y. Liu, Y. Tang, J.B. Goodenough, J.-M. Lee, Exploring indium-based ternary thiospinel as conceivable high-potential air-cathode for rechargeable Zn-air batteries, *Adv. Energy Mater.* 8 (2018) 1802263.
- [10] H.-F. Wang, C. Tang, Q. Zhang, A review of precious-metal-Free bifunctional oxygen electrocatalysts: rational design and applications in Zn–air batteries, *Adv. Funct. Mater.* 28 (2018) 1803329.
- [11] H. Jiang, Y. Liu, W. Li, J. Li, Co nanoparticles confined in 3D nitrogen-doped porous carbon foams as bifunctional electrocatalysts for long-life rechargeable Zn-air batteries, *Small* 14 (2018) 1703739.
- [12] Y.P. Zhu, C. Guo, Y. Zheng, S.Z. Qiao, Surface and interface engineering of noble-metal-free electrocatalysts for efficient energy conversion processes, *Acc. Chem. Res.* 50 (2017) 915–923.
- [13] L. Ma, S. Chen, Z. Pei, Y. Huang, G. Liang, F. Mo, Q. Yang, J. Su, Y. Gao, J.A. Zapien, C. Zhi, Single-site active iron-based bifunctional oxygen catalyst for a compressible and rechargeable zinc-air battery, *ACS Nano* 12 (2018) 1949–1958.
- [14] I.S. Amiinu, X. Liu, Z. Pu, W. Li, Q. Li, J. Zhang, H. Tang, H. Zhang, S. Mu, From 3D ZIF nanocrystals to Co-Nx/C nanorod array electrocatalysts for ORR, OER, and Zn-air batteries, *Adv. Funct. Mater.* 28 (2018) 1704638.
- [15] G. Fu, X. Yan, Y. Chen, L. Xu, D. Sun, J.-M. Lee, Y. Tang, Boosting bifunctional oxygen electrocatalysis with 3D graphene aerogel-supported Ni/MnO particles, *Adv. Mater.* 30 (2018) 1704609.
- [16] Z. Pei, H. Li, Y. Huang, Q. Xue, Y. Huang, M. Zhu, Z. Wang, C. Zhi, Texturing in situ: N, S-enriched hierarchically porous carbon as a highly active reversible oxygen electrocatalyst, *Environ. Sci.* 10 (2017) 742–749.
- [17] C. Hu, L. Dai, Multifunctional carbon-based metal-free electrocatalysts for simultaneous oxygen reduction, oxygen evolution, and hydrogen evolution, *Adv. Mater.* 29 (2017) 1604942.
- [18] H. Cheng, M.-L. Li, C.-Y. Su, N. Li, Z.-Q. Liu, Cu-Co bimetallic oxide quantum dot decorated nitrogen-doped carbon nanotubes: a high-efficiency bifunctional oxygen electrode for Zn-air batteries, *Adv. Funct. Mater.* 27 (2017) 1701833.
- [19] G. Fu, Y. Liu, Y. Chen, Y. Tang, J.B. Goodenough, J.-M. Lee, Robust N-doped carbon aerogels strongly coupled with iron–cobalt particles as efficient bifunctional catalysts for rechargeable Zn-air batteries, *Nanoscale* 10 (2018) 19937.
- [20] X. Zhu, T. Jin, C. Tian, C. Lu, X. Liu, M. Zeng, X. Zhuang, S. Yang, L. He, H. Liu, S. Dai, In situ coupling strategy for the preparation of FeCo alloys and Co₄N hybrid for highly efficient oxygen evolution, *Adv. Mater.* 29 (2017) 1704091.
- [21] Y. Fu, H.-Y. Yu, C. Jiang, T.-H. Zhang, R. Zhan, X. Li, J.-F. Li, J.-H. Tian, R. Yang, NiCo alloy nanoparticles decorated on N-doped carbon nanofibers as highly active and durable oxygen electrocatalyst, *Adv. Funct. Mater.* 28 (2018) 1705094.
- [22] L. Yang, X. Zeng, D. Wang, D. Cao, Biomass-derived FeNi alloy and nitrogen-co-doped porous carbons as highly efficient oxygen reduction and evolution bifunctional electrocatalysts for rechargeable Zn-air battery, *Energy Storage Mater.* 12 (2018) 277–283.
- [23] Z. Pei, J. Gu, Y. Wang, Z. Tang, Z. Liu, Y. Huang, Y. Huang, J. Zhao, Z. Chen, C. Zhi, Component matters: paving the roadmap toward enhanced electrocatalytic performance of graphitic C₃N₄-based catalysts via atomic tuning, *ACS Nano* 11 (2017) 6004–6014.
- [24] X. Han, X. Wu, C. Zhong, Y. Deng, N. Zhao, W. Hu, NiCo₂S₄ nanocrystals anchored on nitrogen-doped carbon nanotubes as a highly efficient bifunctional electrocatalyst for rechargeable zinc-air batteries, *Nano Energy* 31 (2017) 541–550.
- [25] D. Yang, L. Zhang, X. Yan, X. Yao, Recent progress in oxygen electrocatalysts for zinc-air batteries, *Small Methods* 1 (2017) 1700209.
- [26] F.L. Meng, K.H. Liu, Y. Zhang, M.M. Shi, X.B. Zhang, J.M. Yan, Q. Jiang, Recent advances toward the rational design of efficient bifunctional air electrodes for rechargeable Zn-air batteries, *Small* 14 (2018) 1703843.
- [27] B.Y. Guan, Y. Lu, Y. Wang, M. Wu, X.W.D. Lou, Porous Iron–Cobalt alloy/nitrogen-doped carbon cages synthesized via pyrolysis of complex metal–organic framework hybrids for oxygen reduction, *Adv. Funct. Mater.* 28 (2018) 1706738.
- [28] L. Wei, H.E. Karahan, S. Zhai, H. Liu, X. Chen, Z. Zhou, Y. Lei, Z. Liu, Y. Chen, Amorphous bimetallic oxide–graphene hybrids as bifunctional oxygen electrocatalysts for rechargeable Zn-air batteries, *Adv. Mater.* 29 (2017) 1701410.
- [29] S. Cai, Z. Meng, H. Tang, Y. Wang, P. Tsakaros, 3D Co-N-doped hollow carbon spheres as excellent bifunctional electrocatalysts for oxygen reduction reaction and oxygen evolution reaction, *Appl. Catal. B: Environ.* 217 (2017) 477–484.
- [30] S. Li, C. Cheng, X. Zhao, J. Schmidt, A. Thomas, Active salt/silica-templated 2D mesoporous FeCo-Nx-carbon as bifunctional oxygen electrodes for zinc-air batteries, *Angew. Chem. Int. Ed.* 57 (2018) 1856–1862.
- [31] S. Liu, Z. Wang, S. Zhou, F. Yu, M. Yu, C.-Y. Chiang, W. Zhou, J. Zhao, J. Qiu, Metal–organic framework -derived hybrid carbon nanocages as a bifunctional electrocatalyst for oxygen reduction and evolution, *Adv. Mater.* 29 (2017) 1700874.
- [32] L. Yang, X. Zeng, W. Wang, D. Cao, Recent progress in MOF-derived, heteroatom-doped porous carbons as highly efficient electrocatalysts for oxygen reduction reaction in fuel cells, *Adv. Funct. Mater.* 28 (2018) 1704537.
- [33] H. Yang, X. Wang, Secondary -component incorporated hollow MOFs and derivatives for catalytic and energy -related applications, *Adv. Mater.* (2018) 1800743.
- [34] J. Nai, X.W. Lou, Hollow structures based on prussian blue and its analogs for electrochemical energy storage and conversion, *Adv. Mater.* (2018) 1706825.
- [35] M. Khalid, A.M.B. Honorato, H. Varela, L. Dai, Multifunctional electrocatalysts derived from conducting polymer and metal organic framework complexes, *Nano Energy* 45 (2018) 127–135.
- [36] M. Zeng, Y. Liu, F. Zhao, K. Nie, N. Han, X. Wang, W. Huang, X. Song, J. Zhong, Y. Li, Metallic cobalt nanoparticles encapsulated in nitrogen-enriched graphene shells: its bifunctional electrocatalysis and application in zinc-air batteries, *Adv. Funct. Mater.* 26 (2016) 4397–4404.
- [37] L. Han, X.-Y. Yu, X.W. Lou, Formation of prussian-blue-Analog nanocages via a direct etching method and their conversion into Ni-Co-Mixed oxide for enhanced oxygen evolution, *Adv. Mater.* 28 (2016) 4601–4605.
- [38] W. Ahn, M.G. Park, D.U. Lee, M.H. Seo, G. Jiang, Z.P. Cano, F.M. Hassan, Z. Chen, Hollow multivoid nanocuboids derived from ternary Ni-Co-Fe prussian blue analog for dual-electrocatalysis of oxygen and hydrogen evolution reactions, *Adv. Funct. Mater.* 28 (2018) 1802129.
- [39] J. Nai, B.Y. Guan, L. Yu, X.W.D. Lou, Oriented assembly of anisotropic nanoparticles into frame-like superstructures, *Sci. Adv.* 3 (2017) e1700732.
- [40] Z. Wang, S. Peng, Y. Hu, L. Li, T. Yan, G. Yang, D. Ji, M. Srinivasan, Z. Pan, S. Ramakrishna, Cobalt nanoparticles encapsulated in carbon nanotube-grafted nitrogen and sulfur co-doped multichannel carbon fibers as efficient bifunctional oxygen electrocatalysts, *J. Mater. Chem. A* 5 (2017) 4949–4961.
- [41] E. Hu, X.-Y. Yu, F. Chen, Y. Wu, Y. Hu, X.W. Lou, Graphene layers-wrapped Fe/Fe₅C₂ nanoparticles supported on N-doped graphene nanosheets for highly efficient oxygen reduction, *Adv. Energy Mater.* 8 (2018) 1702476.
- [42] C.-Y. Su, H. Cheng, W. Li, Z.-Q. Liu, N. Li, Z. Hou, F.-Q. Bai, H.-X. Zhang, T.-Y. Ma, Atomic modulation of FeCo–nitrogen–carbon bifunctional oxygen electrodes for

rechargeable and flexible all-solid-state zinc–air battery, *Adv. Energy Mater.* 7 (2017) 1602420.

[43] Y. Jiang, C. Zhou, J. Liu, A non-polarity flexible asymmetric supercapacitor with nickel nanoparticle@ carbon nanotube three-dimensional network electrodes, *Energy Storage Mater.* 11 (2018) 75–82.

[44] G. Fu, Z. Cui, Y. Chen, Y. Li, Y. Tang, J.B. Goodenough, Ni₃Fe-N doped carbon sheets as a bifunctional electrocatalyst for air cathodes, *Adv. Energy Mater.* 7 (2017) 1601172.

[45] Y. Jiang, L. Zou, J. Cheng, Y. Huang, Z. Wang, B. Chi, J. Pu, J. Li, Gadolinium doped ceria on graphene cathode with enhanced cycle stability for non-aqueous lithium–oxygen batteries, *J. Power Sources* 400 (2018) 1–8.

[46] P. Liu, D. Gao, W. Xiao, L. Ma, K. Sun, P. Xi, D. Xue, J. Wang, Self-powered water-splitting devices by core-shell NiFe@ N-graphite-based Zn–air batteries, *Adv. Funct. Mater.* 28 (2018) 1706928.

[47] H. Jiang, Y. Liu, W. Li, J. Li, Co nanoparticles confined in 3D nitrogen-doped porous carbon foams as bifunctional electrocatalysts for long-life rechargeable Zn–air batteries, *Small* 14 (2018) 1703739.

[48] C. Tang, Q. Zhang, Nanocarbon for oxygen reduction electrocatalysis: dopants, edges, and defects, *Adv. Mater.* 29 (2017) 1604103.

[49] G. Jia, W. Zhang, G. Fan, Z. Li, D. Fu, W. Hao, C. Yuan, Z. Zou, Three-dimensional hierarchical architectures derived from surface-mounted metal-organic framework membranes for enhanced electrocatalysis, *Angew. Chem. Int. Ed.* 56 (2017) 13781–13785.

[50] H. Wang, W. Wang, M. Asif, Y. Yu, Z. Wang, J. Wang, H. Liu, J. Xiao, Cobalt ion-coordinated self-assembly synthesis of nitrogen-doped ordered mesoporous carbon nanosheets for efficiently catalyzing oxygen reduction, *Nanoscale* 9 (2017) 15534–15541.

[51] C.L. Zhang, B.R. Lu, F.H. Cao, Z.L. Yu, H.P. Cong, S.H. Yu, Hierarchically structured Co₃O₄@ carbon porous fibers derived from electrospun ZIF-67/PAN nanofibers as anodes for lithium ion batteries, *J. Mater. Chem. A* 6 (2018) 12962–12968.

[52] K.N. Dinh, P. Zheng, Z. Dai, Y. Zhang, R. Dangol, Y. Zheng, B. Li, Y. Zong, Q. Yan, Ultrathin porous NiFeV ternary layer hydroxide nanosheets as a highly efficient bifunctional electrocatalyst for overall water splitting, *Small* 14 (2018) 1703257.